

# Phase-change memory as a memristive system: The state equations and dynamic route maps

Francesco Marrone<sup>1,\*</sup>, Jacopo Secco<sup>1</sup>, Benedikt Kersting<sup>2</sup>, Manuel Le Gallo<sup>2</sup>, Fernando Corinto<sup>1</sup>, Abu Sebastian<sup>2</sup>, and Leon O. Chua<sup>3</sup>

<sup>1</sup>Politecnico di Torino, Department of Electronics and Telecommunications, Torino, 10129, Italy

<sup>2</sup>IBM Research, Rüschlikon, 8803, Switzerland

<sup>3</sup>University of California, Department of Electrical Engineering and Computer Sciences, Berkeley, 94720, CA, USA

\*francesco.marrone@polito.it

## ABSTRACT

*Phase Change Memory* (PCM) is an emerging technology exploiting the rapid and reversible phase transition of certain chalcogenides to realize nanoscale memory elements. PCM devices are being explored as non-volatile storage-class memory and as computing elements for in-memory and neuromorphic computing. It is well-known that PCM exhibits several characteristics of a memristive device. In this work, based on the essential physical attributes of PCM devices, we exploit the concept of *Dynamic Route Map* (DRM) to capture the complex physics underlying these devices to describe as memristor defined by a state-dependent Ohm's law. The efficacy of the DRM has been proven by comparing numerical results with experimental data obtained on PCM devices.

## Introduction

Phase Change Memory (PCM) devices encode information on the phase configuration of a layer of material sandwiched between two metallic electrodes. This class of materials, typically compounds of Ge, Te and Sb exhibit a high electric conductivity in the crystalline phase and a much lower conductivity in the amorphous phase. A prototypical mushroom-type PCM<sup>1</sup> is schematically shown in Figure 1a. By modulating the size of the amorphous region by the application of suitable electrical pulses, it is possible to achieve a continuum of resistance or conductance states.

PCM devices exhibit intriguing nonlinear dynamical behavior arising from a complex interaction among thermal, electrical and structural dynamics.<sup>2</sup> In the so called low-field *OFF-state*, PCM devices' conduction goes, for increasing applied electric fields, through ohmic, exponential and super-exponential regimes<sup>3</sup>. In the high-field *ON-state*, conduction through the amorphous phase is metal-like and the global flow of electrons in the PCM cell becomes dominated by the amorphous-crystalline Schottky barrier<sup>4</sup>.

The quite complex transition between the OFF and ON states happens via the so called threshold switching event. This is mainly dominated by a feedback-driven thermo-electrical mechanism<sup>5</sup>. As the conductivity increases due to the field-induced barrier lowering between two close coulombic centers, the temperature rises. When the temperature is high enough, it strongly lowers the activation energy and this in turn allows more electrons to flow through the material increasing further the conductivity. This, in a very short time, leads to the threshold-switching event. Threshold switching is of fundamental importance in the operation of PCM devices because it enables the fast *WRITE* operation via a high temperature increase. Inside an appropriate range of temperature the *WRITE* operation takes either the form of a *SET* operation or a *RESET* operation<sup>6</sup>. The former increases the low-field conductivity by shrinking the size of the amorphous region via the crystallization process while the latter increases the amorphous mushroom radius via the *melt-quenching* process when the temperature inside the cell exceeds the *GST* melting temperature  $T_{MELT} \approx 877K$ .

Accurate physical models exploiting integro-differential equations have been derived to capture the peculiar characteristic of the different operating conditions in PCM devices and then numerical analysis is essential to accurately describe the experimental observations<sup>5</sup>. However, it will be very interesting to describe the PCM device dynamics described as a memristive system as introduced in 1976 by S. Kang and L. O. Chua. The pinched *current-voltage* loop characteristics shown by PCM devices under bipolar periodic input, as exemplified in Figure 1b, clearly casts them in the memristive<sup>7</sup> systems class. In this work, our objective is to represent PCM devices via a state-dependent Ohm's law, that is the Ohm's law  $v = R(\mathbf{x}, i)i$  linking voltage  $v$  across and current  $i$  through the two-terminal memristor and a state equation  $\dot{\mathbf{x}} = f(\mathbf{x}, i)$  governing the dynamics of internal state variables  $\mathbf{x}$ . The use of the memristor state-dependent Ohm's law permit to unfold complex dynamics in PCM cells via the concepts of Dynamic Route Map (DRM) and the Power-Off-Plot (POP)<sup>8</sup>. When the state variable is scalar ( $x \in \mathbf{R}$ ), the

DRM consists in the plot of  $f(x, i)$  in the plane  $(\dot{x}, x)$ ; each DRM is parametrized by the input  $i$  and then a family of curves span the whole plane  $(\dot{x}, x)$ . If  $i = 0$  then the DRM results into the POP and describe the long-term behavior of the memristor devices and its memory properties. Such a circuit-theoretic model is capable of accurately describing electrical measurements and embedding the device physics in some key parameters. The use of DRMs, in addition, has been found to be a useful modeling method in the last years for similar devices. The work of Ascoli *et al.*<sup>9</sup> where it has been proven that the use of such technique can be exploited to investigate theoretically all the scenarios of the switching dynamics in memristors. Subsequently other works have shown how DRMs can render a powerful tool for modeling of other devices such as ReRAMs, or of complex systems such as *Cellular Nonlinear Networks*<sup>10,11</sup>. In this work, the experimental data taken from PCM devices shows how the modeling of this elements can be successfully conducted through this technique.

## Materials and Methods

### Phase-change memory devices

The PCM devices used in this study were of mushroom-type. The phase-change material was doped  $\text{Ge}_2\text{Sb}_2\text{Te}_5$ . The bottom electrode had a radius of  $\approx 20$  nm and length of  $\approx 65$  nm. The phase change material was  $\approx 100$  nm thick and extended to the top electrode, the radius of which was  $\approx 100$  nm.

### Experimental details

The experimental setup included an arbitrary waveform generator (AWG) to apply the desired input stimulus and a Digital Storage Oscilloscope (DSO) to measure the current  $I$  and the applied voltage  $V_{\text{applied}}$ . The DSO acquired all the signals at a sampling frequency  $f_s = 2.5$  GHz.  $V_{\text{applied}}$  was directly measured by the DSO from the AWG. The resulting current that flows through the device was measured by having an isolated linear resistor,  $R_s$  which was placed in close proximity to the device. Given the length of the wires ( $\approx 60$  cm) and the involved time scales, the phase shift of current with respect to the  $V_{\text{applied}}$  signal had to be taken into account. The delay was estimated to be  $\approx 6.4$  ns.

Before performing each measurement, the cell was reset with a  $950 \mu\text{A}$  amplitude square pulse of  $1 \mu\text{s}$  duration and sharp leading and trailing edges of  $7.5$  ns each. The reset was intended to create an amorphous dome of  $u_a \approx 40$  nm. This was estimated by fitting the resulting  $I - V$  characteristics to a transport model proposed by Ielmini and Zhang<sup>12</sup>. A train of interleaved write and read pulses were applied  $20 \mu\text{s}$  after applying the reset pulse. Each write pulse with  $7.5$  ns leading and trailing edges had an amplitude of  $\approx 2.93$  V and a variable duration ranging between  $25$  ns and  $121$  ns). Each writing pulse was followed, after  $25$  ns, by a read ramp voltage pulse of  $0.5$  V peak value and  $50$  ns duration. The reading voltage ramps had a  $7.5$  ns trailing edge and were followed by a new writing pulse after  $25$  ns.

## Results

### Memristive state equations

An useful block representation of the convoluted interconnections between the various phenomena is reported in Figure 2. It includes, on first approximation, only two state variables  $T_{\text{int}}$  and  $u_a$  while the output current  $I$  (and the internally dissipated power  $P = V_{\text{cell}}I$ ) can be expressed via an algebraic relation linking the state variables, the input cell voltage drop  $V_{\text{cell}}$  and the ambient temperature  $T_{\text{AMB}}$ .

### Thermal dynamic subsystem

The thermal dynamic Subsystem is the simplest of the three blocks (see Figure 3a). The PCM cell state variable,  $T_{\text{int}}$ , which is the temperature at the Amorphous/Crystalline Interface (ACI) that governs the crystallization process, is obtained as  $T_{\text{int}} = T_{\text{AMB}} + T_{\text{SH}}$  where  $T_{\text{AMB}}$  is the ambient temperature and  $T_{\text{SH}}$ , the cell Joule self-heating temperature increment. This in turn is the intrinsic dynamical component of  $T_{\text{int}}$  which obeys the Ordinary Differential Equation (ODE)

$$\frac{d}{dt}T_{\text{SH}}(t) = \frac{1}{\tau_{\text{th}}}(R_{\text{th}}(u_a(t))P - T_{\text{SH}}(t)) \quad (1)$$

where  $\tau_{\text{th}} = R_{\text{th}}(u_a(t))C_{\text{th}}(u_a(t))$  is the thermal time constant and  $R_{\text{th}}(u_a(t))$ , shown in Figure 4a, is the amorphous-thickness-dependent thermal resistance of the amorphous-phase mushroom which was estimated via FEM simulations as the thermal resistance between the ACI and the external environment. A good linear approximation of  $R_{\text{th}}(u_a)$  can be given, in the blocked BE electrode condition, as

$$R_{\text{th}}(u_a(t)) = -\kappa u_a(t) + R_{\text{th},0} \quad (2)$$

where,  $\kappa \approx -0.024 \frac{\text{K}}{\mu\text{Wnm}}$  and  $R_{\text{th},0} \approx 1.908 \frac{\text{K}}{\mu\text{W}}$ . Being the thermal capacitance  $C_{\text{th}}(u_a(t))$  directly proportional to the amorphous-phase mushroom volume, given the linearly decreasing approximation of  $R_{\text{th}}(u_a(t))$ , it is reasonable to assume  $\tau_{\text{th}} \approx \text{const.}$

This was found to be on the order of tens of nanoseconds<sup>13</sup>. Considering the input variables to be slowly varying then (1) can be reduced to an algebraic equation as

$$T_{SH}(t) = R_{th}(u_a(t))P \quad (3)$$

hence the interface temperature  $T_{int} = T_{AMB} + T_{SH}$  is assumed to instantly vary with the input power  $P = IV_{cell}$  as shown by the circuit representation in Figure (3b).

### Structural dynamic subsystem

The structural dynamic subsystem describes the evolution of the state variable,  $u_a(t)$ , which is the effective amorphous thickness of the amorphous-phase. This differs from the amorphous thickness, being the latter the distance of the ACI from the center of the amorphous-phase mushroom<sup>14</sup>. The evolution of  $u_a(t)$  is dictated by the temperature-driven crystallization dynamics accordingly to the ODE

$$\frac{d}{dt}u_a(t) = -v_g(T_{int}(t)) \quad (4)$$

where  $u_a \in [0, 80]nm$ . The crystal growth velocity  $v_g$  was estimated<sup>15</sup> and is reported in Figure 4b. A Gaussian approximation<sup>16</sup> of  $v_g(T_{int})$  has also already been proposed as

$$v_g(T_{int}) = A_{v_g} \exp\left(-\left(\frac{T_{int} - T_0}{\sigma_T}\right)^2\right) \quad (5)$$

$A_{v_g} \approx 0.57 \frac{nm}{ns}$ ,  $T_0 \approx 749K$  and  $\sigma_T \approx 98K$ . Changes of the amorphous phase's material characteristics are not taken into account in this model. In the experimental data studied later this effect was considered negligible due to a narrow observation time window.

### Electrical subsystem

The last and most complex part of the block decomposition of the PCM cell dynamical system is the electrical algebraic subsystem. This encapsulates the conduction model in the amorphous-phase *GST*. More and more refined models have been developed over the years to explain how the two state variables ( $u_a, T_{int}$ ) influence the electron conduction through the material. A certain class of these models hold valid in specific electric-field domains. Introducing  $F_T$  as the transition field

$$F_T = \frac{q_e}{\pi \epsilon_r \epsilon_0 s^2}$$

where  $q_e$  is the fundamental electron charge,  $\epsilon_r \approx 10$  is the relative permittivity of the amorphous phase,  $\epsilon_0$  is the vacuum permittivity and  $s$  is the average distance between defects in the amorphous phase.

The simple Poole<sup>17</sup> conduction law well describes the conduction in the low to moderate electric field domain ( $F = \frac{V_{cell}}{u_a} \ll F_T$ ) while in the high field domain ( $F \gg F_T$ ) the Pool-Frenkel<sup>181920</sup> model gives the best approximation.

The 3D Poole-Frenkel<sup>2122</sup> emission of carriers from a two-center Coulomb potential was shown to best model in an unified manner the conduction in *GST* material for the whole range of fields  $F$  in the below threshold condition. According to this model, the density of free carriers under an applied field  $F = \frac{V_{cell}}{u_a}$  at an interface temperature,  $T_{int}$  is

$$n(F, T_{int}) = \frac{K}{2} \int_0^\pi \exp\left(-\frac{E_a(T_{int}) - E_{PF}(F, \theta)}{k_B T_{int}}\right) \sin(\theta) d\theta$$

where  $E_a(T_{int})$  is the interface temperature dependent activation energy

$$E_a(T_{int}) = E_{a,0} - \frac{aT_{int}^2}{b + T_{int}}$$

and  $E_{PF}(F, \theta)$  is the the energy barrier lowering between two adjacent potential wells due to the Poole-Frenkel effect and is computed as

$$E_{PF}(F, \theta) = -\max_r \Phi(r, \theta, F)$$

where  $\Phi(r, \theta, F) = -qFrcos(\theta) - \frac{\beta^2}{4q} \left(\frac{1}{r} + \frac{1}{s-r}\right) + \frac{\beta^2}{qs}$  is the electrical potential profile where  $\beta = \frac{q^2}{\sqrt{q\pi\epsilon_r\epsilon_0}}$  Conductivity of the amorphous phase per unit of area can be then computed as

$$\sigma(F, T_{int}) = q\mu(F)n(F, T_{int})$$

where  $\mu(F)$  is the field dependent carrier mobility given by  $\mu(F) = \frac{\mu_0}{\sqrt{1+(\mu_0 F/v_{sat})^2}}$ . The current density  $j(F, T_{int})$  can be computed as  $j(F, T_{int}) = \sigma(F, T_{int})F$ . and the current flowing through the cell can be found by simply multiplying the current density  $j(F, T_{int})$  times the effective bottom electrode contact area  $A$  which is calculated through the effective bottom electrode radius and not the physical radius of the heater,  $I(F, T_{int}) = Aj(F, T_{int})$ . Even if the 3D Poole-Frenkel emission model describes the conduction up to the threshold switching event nonetheless it still cannot accurately capture the above threshold conduction after the amorphous phase is switched on.

PCM devices can be *reset* to high resistance state via relatively high current pulses which increases the temperature up to the melting temperature  $T_{MELT}$ . Higher currents flowing through the device imply higher power dissipations which, in turn, imply that  $T_{MELT}$  is reached further away from the BE. This creates an amorphous mushroom whose effective amorphous thickness  $u_a$  is proportional to the reset current  $I_{RESET}$  as shown in Figure 5a where  $(i - v)$  characteristics under a ramp input are plotted for different reset conditions reported in the figure legend.

### State dependent Ohm's Law

Read operation refers to the retrieval of the phase-configurational information (long-term memory state) by application of a low amplitude current pulse. Under the hypothesis of fully blocked BE ( $u_a > 0$ ) and very *low-field* ( $F = \frac{V_{cell}}{u_a} \rightarrow 0$ ), the voltage can be well approximated by a linear relation  $V_{cell} = R_m(u_a, T_{int})I$ , as shown in Figure 5b, where the memristance  $R_m(u_a, T_{int})$  is given by

$$R_m(u_a, T_{int}) = K' u_a \exp\left(\frac{E_a(T_{int})}{k_B T_{int}}\right) \quad (6)$$

being  $k_B$  the Boltzmann constant,  $E_a(T_{int})$ , the temperature-dependent activation energy and  $K' = \frac{1}{\pi r_{BE}^2 q_e K \mu_0}$ . This expression for the memristance  $R_m(u_a, T_{int})$  can readily be derived from the Taylor series expansion of the Poole conduction model.

When the phase-change material sandwiched between the metal electrodes is bias at high field, it goes into a very low resistance state independent of the state variable  $u_a$ . As shown in Figure (5c) and Figure (6), the voltage drop  $V_{cell}$  is confined to a narrow voltage band around  $V_{cell,ON} \approx 0.8V$ . This is because in the very-low after-switching resistance state the conduction is dominated by the barrier at the metal-semiconductor contact junction and the resistance of the metallic bottom electrode. This enables, for the purpose of this study, the simplification of the complex conduction mechanism to a simple nonlinear current-controlled resistor whose behavior for high enough currents can be well approximated by an ideal voltage generator of value  $V_{cell,ON}$ .

The two-domain approximation given in the previous subsections can be summarized in the following state-dependent Ohm's Law (in a general configuration reported in Figure (5d))

$$V_{cell} \approx \begin{cases} R_m(u_a, T_{int})I & I \ll I_{TH} \\ 0.8V & I \gg I_{TH} \end{cases} \quad (7)$$

where the well-below-threshold-switching model ( $I \ll I_{TH}$ ), portrayed with circuitual symbolism in Figure (5e), gives a good approximation for the information recovery phase and the well-above-threshold-switching model ( $I \gg I_{TH}$ ), depicted with circuitual symbolism in Figure (5f), is intended to capture the cell power dissipation during the write phase. This is of fundamental relevance to predict how the internal state variables ( $u_a, T_{int}$ ) are evolving during the information storing phase and thus come very handy to compute the Dynamic Route Maps.

### Dynamic route maps

Considering the PCM element as current controlled, a set of simulations were performed in order to compute the DRMs of a cell with equal characteristics to the one used to perform the measurements. The DRM calculation was done by tuning the current  $I$  ranging from  $I = 150 \mu A$  to  $650 \mu A$ . The calculations were performed posing combining Equations 4 and 5 and are shown in Figure 7. All the plotted DRMs refer to an initial condition of  $u_a = 40$  nm and each plot corresponds to a different continuous current flowing through the cell.

It can be noted that the computation of the DRMs took into account a slight numerical correction with respect to the relation  $R_{th}(u_a(t))$  described in 2 and shown in Figure 4a. The added correction is intended to avoid the numerical approximations generated by the FEM simulations done to calculate the  $R_{th}(u_a(t))$  relation. The entity of the correction was calculated directly on the experimental data regarding the measurements on the PCM cell, as it will be shown later in this paper. The results of the simulation show that given a specific initial condition on  $u_a$ , the resulting size of the GST mushroom will depend on the current flowing in the device. This is due to an increase of  $T_{int}$  due to an increase of the dissipated power  $P$  as shown in Equation 1. For instance, it can be noted the different dynamics of the GST in the cell for increasing values of current. For

$I = 650 \mu\text{A}$  the thickness of the amorphous region will not reach 0 but it will block its regression at approximately 5.5 nm, while for instance, a current of  $I = 450 \mu\text{A}$  will make the amorphous region shrink completely. This phenomenon can easily be described referring to Figure 4b. As mentioned earlier, increasing the current, leads to an increase of  $T_{\text{int}}$ , which leads to a block of the GST crystallization, consequently blocking its regression. In the presented model, this means a fraction of the material close to the BE is molten again at  $650 \mu\text{A}$  because  $v_g$  drops to zero only for  $T_{\text{int}} > T_{\text{melt}}$  as shown in Figure (4b).

With the same method used to calculate the theoretical DRMs shown in Figure 7, the dynamic routes were obtained for experimental data regarding measurements performed on the PCM cell. Figure 8 shows a representative set of three of the measurements performed. The measurements differ from each other by the pulse duration  $W$  and the number of pulses of the high current writing signal: three pulses of  $W = 121\text{ns}$  for Figure 8a, six pulses of  $W = 42\text{ns}$  for Figure 8b and seven pulses of  $W = 25\text{ns}$  for Figure 8c. The first column of Figure 8 shows the collection of the voltage drops on the cell, which can be noted that settle at  $V_{\text{cell}} \approx 0.8\text{V}$  (solid blue line in the graphs) for each given pulse after a very short transient, consistently with the data shown in Figure 6. In the same graphs in the first column (traced by a solid red line) is plotted the dissipated power  $P$ , which stays constant at each WRITE pulse. The reduction of  $u_a$  is measured in the READ operation by the change of  $R_m(u_a, T_{\text{int}})$  as it is suggested by the data displayed in the middle column of Figure 8. In this column are showed the  $IV$  curves measure when applied the triangular current read pulse (applied between each write pulse as described in the Materials and Methods Section of this paper. For all the readings the Dynamic routes were computed and are displayed in the right column of Figure 8.

Once the dynamic routes have been calculated parting from the experimental data, the same experiments performed on the PCM cell have been simulated on a computational environment using the characteristic equations for these devices. The result of these simulations is shown in Figure 12. Figures 12a, 12b and 12c are referred to the measurements shown in Figures 8a, 8b and 8c, respectively. The comparison between the experimental measurements and the obtained results of the simulations (superimposed black lines) in the  $IV$  curves plotted in the first column. The correction to the  $R_{\text{th}}(u_a(t))$  relation described in 2, was numerically obtained comparing the results. The correction, under a physical point of view, can be considered as a fine tuning of the estimation of the time constant  $\tau_{\text{th}}$ , introduced in the dynamic thermal circuit of the PCM cell shown in Figure 3a. The dynamic routes were then calculated on the simulated circuit as DC pulses (i.e. the value of the constant input power used to compute the DC dynamic routes is the average measured delivered power during the write pulses plateau as reported in Figure 8). The resulting DRMs are reported in the figures of the second column of Figure 12 as solid red lines (DC dynamic routes). It can be noted that these dynamic routes "envelope" the TRANSIENT dynamic routes (i.e. the ones calculated from the experimental data shown in Figure 8, solid blue line). This is due since the TRANSIENT dynamic routes take into consideration also the peaks of the dissipated power  $P$ . Each of the DC dynamic routes, was calculated considering the initial condition of  $u_a(t)$  at the beginning of each pulse train. Each route was traced considering an initial condition  $u_a(t = 0) \approx 40\text{nm}$  in order to generate the same effect of the corresponding reset pulse. From this calculation, it is notable that DRMs are to be considered as a tool for the prediction of the behavior of the PCMs for system design. This is clear when looking at Figure 9, starting from an high resistance *RESET* state associated with  $u_a(t_0) \approx 50\text{nm}$ , the designer can choose to reach three different low resistance states by tuning the SET programming current. The knowledge about how the first order dynamics evolves and the proof that nonzero equilibria of the state variable  $u_a$  exist can be exploited to design programmable circuits such as programmable amplifiers and tunable filters. In the latter case, the knowledge about how the equilibria of  $u_a$  depend on the programming set current  $I_{\text{SET}}$  allows to precisely tune the position of zeros and poles in a completely analog fashion.

Let us consider a simple example where a PCM device is embedded into a passive RLC passband filter as reported in Figure 10. Let us assume the input to be a small signal current  $i_s(t)$  (e.g. current coming from a sensor) and to be measuring the voltage drop  $v_{\text{out}}(t)$  on the parallel RCL. For fixed values of the inductance  $L$  and capacitance  $C$ , the quality factor  $Q = R_m(u_a, T_{\text{int}}) \sqrt{\frac{C}{L}}$  can be tuned to a desired value following the corresponding DRM in Figure 7. Considering the Laplace-transformed port variables  $I_s(s) = \mathcal{L}(i_s(t))$  and  $V_{\text{out}}(s) = \mathcal{L}(v_{\text{out}}(t))$ , Bode plots of the transfer function  $H(s) = \frac{V_{\text{out}}(s)}{I_s(s)}$  are reported in Figure 11 parameterized on the final values reached by following the DRMs in Figure 9. With  $C$  and  $L$  being fixed in the example to  $1 \mu\text{F}$  and  $0.1\text{mH}$  respectively, it is evident how the quality factor,  $Q$ , can be modulated by first resetting the PCM cell and then setting it back with a constant SET current  $I$ .

## Conclusion

Phase-change memory is a highly promising post-CMOS technology that is finding applications as non-volatile memory, compute elements for in-memory and neuromorphic computing and also as components of reconfigurable electronic circuits. In this paper, we have developed a current-controlled memristor model of PCM based on

1. the state-dependent Ohm's law (7) corresponding to the PCM conduction model during READ/WRITE operations
2. the dynamic route maps encompassing the dynamics of the physical variables under different input pulses applied to the

PCM.

One of the crucial information drawn from the DRMs for PCM is the directed design of input current pulses to drive the thickness of the amorphous region ( $u_a(t)$ ) and the corresponding low-field resistance. By exploiting the knowledge gained on the temporal evolution of  $u_a(t)$  (see for instance fig. 7, built using experimental measurements taken on the single elements), suitable current pulses can be chosen to modulate dissipation in analog electronic circuits. As case of study we have presented a PCM-based analog filter. As afore mentioned, exploiting the same technique, it is proven that is also possible to derive the characteristics of the singular device basing its modeling on DRMs, an also through the same technique it is possible to model complex systems that function through the interaction of these elements, as also shown with different devices in the work by Ascoli *et al*<sup>9</sup>. For this last reason this work is to be considered as a significant step towards the inclusion of memristor-based PCM model in automatic design tools for programmable analog circuits and also for tunable synaptic elements in neuromorphic circuitry, overcoming the limitations given by the complex dynamics of these elements.

## References

1. Burr, G. W. *et al.* Phase change memory technology. *J. Vac. Sci. & Technol. B* **28**, 223–262, DOI: [10.1116/1.3301579](https://doi.org/10.1116/1.3301579) (2010).
2. Le Gallo, M. & Sebastian, A. An overview of phase-change memory device physics. *J. Phys. D: Appl. Phys.* **53**, 213002, DOI: [10.1088/1361-6463/ab7794](https://doi.org/10.1088/1361-6463/ab7794) (2020).
3. Nardone, M., Simon, M., Karpov, I. V. & Karpov, V. G. Electrical conduction in chalcogenide glasses of phase change memory. *J. Appl. Phys.* **112**, 071101, DOI: [10.1063/1.4738746](https://doi.org/10.1063/1.4738746) (2012).
4. Kroezen, H. J. *et al.* Schottky barrier formation at amorphous-crystalline interfaces of phase change materials. *Appl. Phys. Lett.* **100**, 094106, DOI: [10.1063/1.3691179](https://doi.org/10.1063/1.3691179) (2012).
5. Le Gallo, M., Athmanathan, A., Krebs, D. & Sebastian, A. Evidence for thermally assisted threshold switching behavior in nanoscale phase-change memory cells. *J. Appl. Phys.* **119**, 025704, DOI: [10.1063/1.4938532](https://doi.org/10.1063/1.4938532) (2016).
6. Faraclas, A., Williams, N., Gokirmak, A. & Silva, H. Modeling of set and reset operations of phase-change memory cells. *IEEE Electron Device Lett.* **32**, 1737–1739, DOI: [10.1109/LED.2011.2168374](https://doi.org/10.1109/LED.2011.2168374) (2011).
7. Chua, L. Memristor—the missing circuit element. *IEEE Transactions on Circuit Theory* **18**, 507–519, DOI: [10.1109/TCT.1971.1083337](https://doi.org/10.1109/TCT.1971.1083337) (1971).
8. Chua, L. Five non-volatile memristor enigmas solved. *Appl. Phys. A* **124**, 563, DOI: [10.1007/s00339-018-1971-0](https://doi.org/10.1007/s00339-018-1971-0) (2018).
9. Ascoli, A., Messaris, I., Tetzlaff, R. & Chua, L. O. Theoretical foundations of memristor cellular nonlinear networks: Stability analysis with dynamic memristors. *IEEE Transactions on Circuits Syst. I: Regul. Pap.* **67**, 1389–1401 (2019).
10. Ascoli, A., Tetzlaff, R., Kang, S.-M. & Chua, L. O. Theoretical foundations of memristor cellular nonlinear networks: a DRM 2-based method to design memcomputers with dynamic memristors. *IEEE Transactions on Circuits Syst. I: Regul. Pap.* **67**, 2753–2766 (2020).
11. Maldonado, D. *et al.* Experimental evaluation of the dynamic route map in the reset transition of memristive ReRAMs. *Chaos, Solitons & Fractals* **139**, 110288 (2020).
12. Ielmini, D. & Zhang, Y. Analytical model for subthreshold conduction and threshold switching in chalcogenide-based memory devices. *J. Appl. Phys.* **102**, 054517, DOI: [10.1063/1.2773688](https://doi.org/10.1063/1.2773688) (2007).
13. Le Gallo, M. *Phase-Change Memory: Device Physics and Application to non-von Neumann Computing*. Ph.D. thesis, ETH Zurich (2017). DOI: [10.3929/ethz-b-000250342](https://doi.org/10.3929/ethz-b-000250342).
14. Sebastian, A., Papandreou, N., Pantazi, A., Pozidis, H. & Eleftheriou, E. Non-resistance-based cell-state metric for phase-change memory. *J. Appl. Phys.* **110**, 084505, DOI: [10.1063/1.3653279](https://doi.org/10.1063/1.3653279) (2011).
15. Sebastian, A., Le Gallo, M. & Krebs, D. Crystal growth within a phase change memory cell. *Nat. Commun.* **5**, 4314, DOI: [10.1038/ncomms5314](https://doi.org/10.1038/ncomms5314) (2014).
16. Secco, J., Corinto, F. & Sebastian, A. Flux-charge memristor model for phase change memory. *IEEE Transactions on Circuits Syst. II: Express Briefs* **65**, 111–114, DOI: [10.1109/TCSII.2017.2701282](https://doi.org/10.1109/TCSII.2017.2701282) (2018).
17. Ongaro, R. & Pillonnet, A. Synthetic theory of poole and poole-frenkel (pf) effects. *IEE Proc. A (Science, Meas. Technol.)* **138**, 127–137(10), DOI: [10.1049/ip-a-3.1991.0018](https://doi.org/10.1049/ip-a-3.1991.0018) (1991).
18. Frenkel, J. On pre-breakdown phenomena in insulators and electronic semi-conductors. *Phys. Rev.* **54**, 647–648 (1938).

19. Shih, Y. H. *et al.* Understanding amorphous states of phase-change memory using frenkel-pooler model. In *2009 IEEE International Electron Devices Meeting (IEDM)*, 1–4, DOI: [10.1109/IEDM.2009.5424229](https://doi.org/10.1109/IEDM.2009.5424229) (2009).
20. Hill, R. M. Poole-frenkel conduction in amorphous solids. *The Philos. Mag. A J. Theor. Exp. Appl. Phys.* **23**, 59–86, DOI: [10.1080/14786437108216365](https://doi.org/10.1080/14786437108216365) (1971).
21. Hartke, J. L. The three-dimensional poole-frenkel effect. *J. Appl. Phys.* **39**, 4871–4873, DOI: [10.1063/1.1655871](https://doi.org/10.1063/1.1655871) (1968).
22. Betti Beneventi, G., Guarino, L., Ferro, M. & Fantini, P. Three-dimensional poole-frenkel analytical model for carrier transport in amorphous chalcogenides. *J. Appl. Phys.* **113**, 044506, DOI: [10.1063/1.4788798](https://doi.org/10.1063/1.4788798) (2013).

## **Acknowledgements (not compulsory)**

### **Author contributions statement**

Francesco Marrone took the experimental data and compiled the mathematical model. Benedikt Kersting helped in the acquisition of the experimental data. Manuel Le Gallo supervised the correctness of the data acquisition procedure. Jacopo Secco contributed in the formulation of the mathematical model and simulations. Fernando Corinto, Abu Sebastian and Leon Chua are the PIs of this project.

### **Additional information**

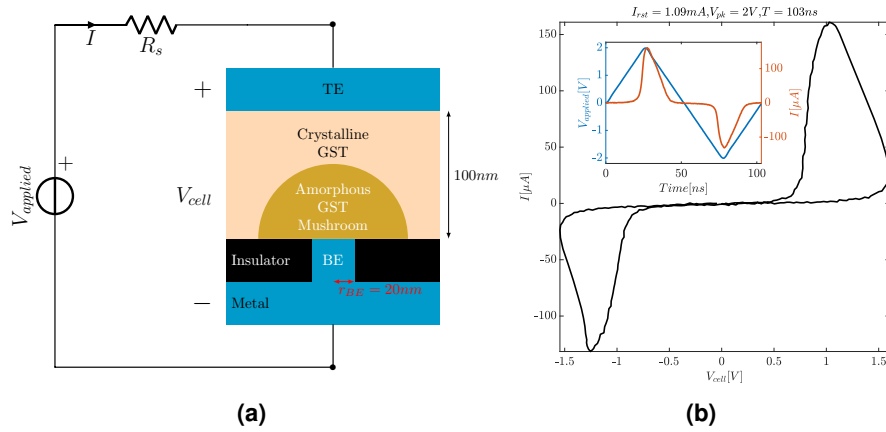


**Figure 1.** (a) Schematic representation of a mushroom-type PCM device operated with a current compliance series resistor  $R_s$ . In the RESET state, the amorphous phase blocks the bottom electrode, and the device is in a high-resistance state. The effective thickness of the amorphous region is denoted by  $u_a(t)$ .  $V_{applied}(t)$  is the externally applied input voltage,  $I(t)$  is the current flowing through the PCM device and  $V_{cell} = V_{applied} - R_s I$  is the intrinsic voltage drop on the device. (b) Measured pinched hysteresis loop for a mushroom PCM device stimulated by a 103 ns period triangular  $V_{applied}$  pulse of 2V peak voltage  $V_{pk}$ .

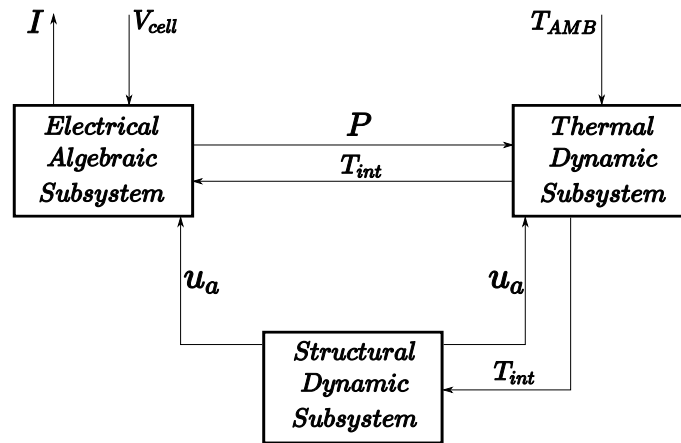


**Figure 2.** Simplified block representation of the PCM device subsystems. The system has two inputs respectively  $V_{cell}(t)$  and  $T_{AMB}$  and one output  $I(t)$ .  $V_{cell}(t)$  is the voltage drop on the PCM device.  $I(t)$  is the current flowing through the device.  $T_{AMB}$  is the ambient temperature the PCM device is operated at.  $P(t)$  is the algebraic electrical power dissipated by the device and computed as the product current  $I(t)$  times voltage  $V_{cell}(t)$ .  $u_a(t)$  is the amorphous mushroom thickness and its evolution is determined by the crystallization dynamics.  $T_{int}(t)$  is the temperature at the amorphous-crystalline interface and its evolution is determined by the heat balance equation.

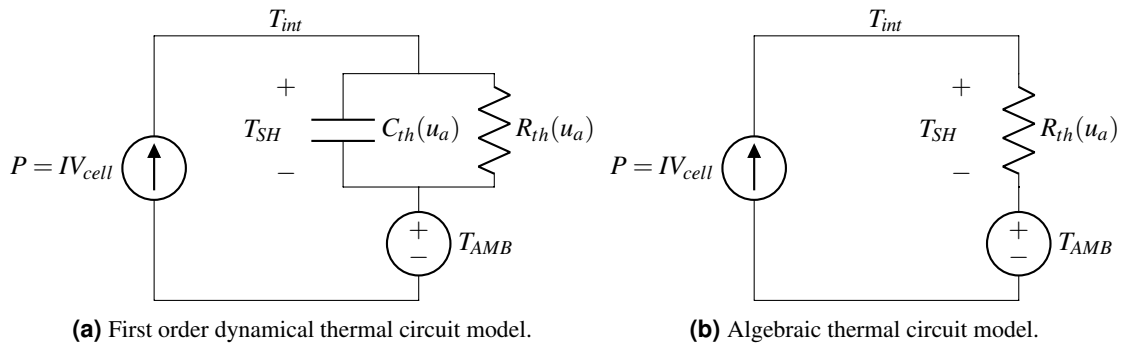


**Figure 3.** (a) First order dynamical thermal circuit that takes into account the presence of  $C_{th}(u_a)$ . Its dynamics can be described through Equation (1). For the sake of the presented model the input signals to the PCM device are considered to be at least twice longer in duration than  $\tau_{th}$ , for this reason it is taken into account (b) described by Equation (3).

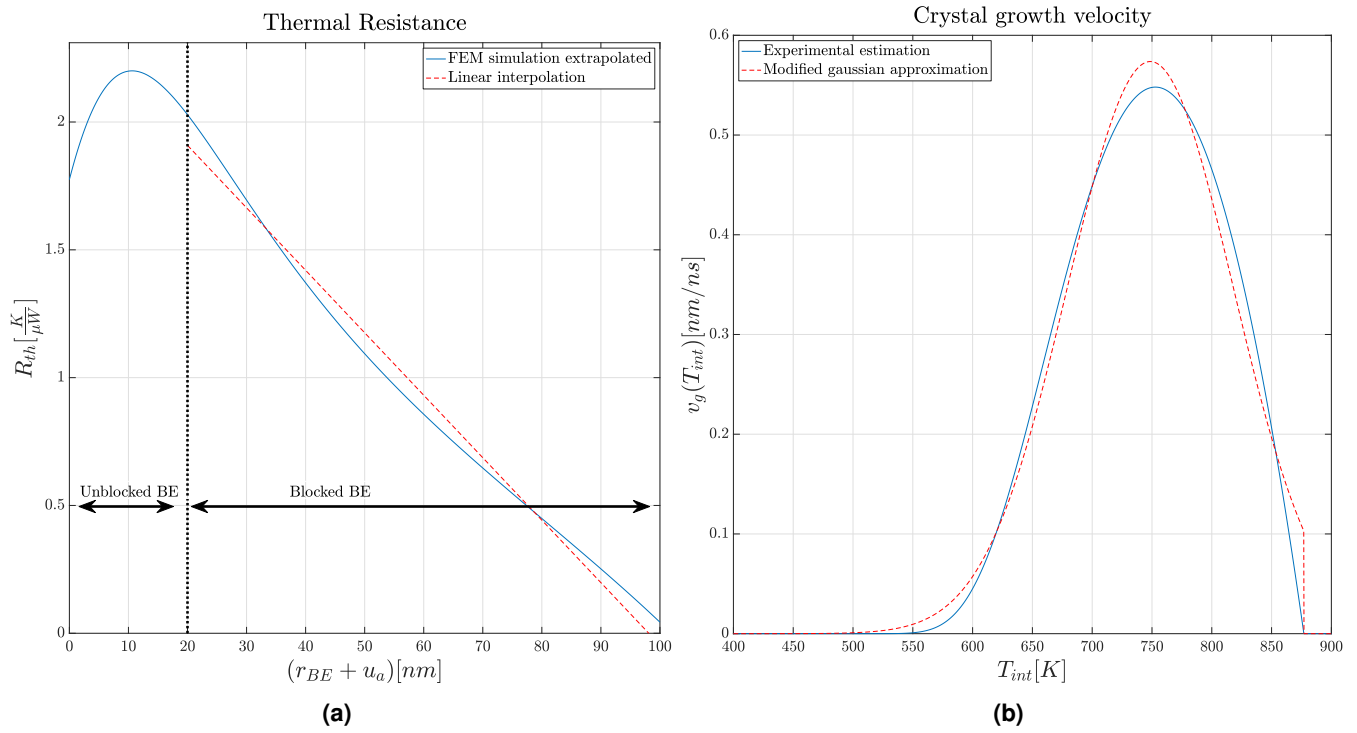


**Figure 4.** (a) in continuous blue the effective thermal resistance, extrapolated from FEM simulations, as a function of the amorphous thickness  $u_a(t)$ . In dashed red the linear approximation of the effective thermal resistance in the blocked BE condition. (b) in continuous blue the experimentally estimated GST crystal growth velocity  $v_g(T_{int})$  as a function of the interface temperature  $T_{int}$ . In dashed red its Gaussian approximation.

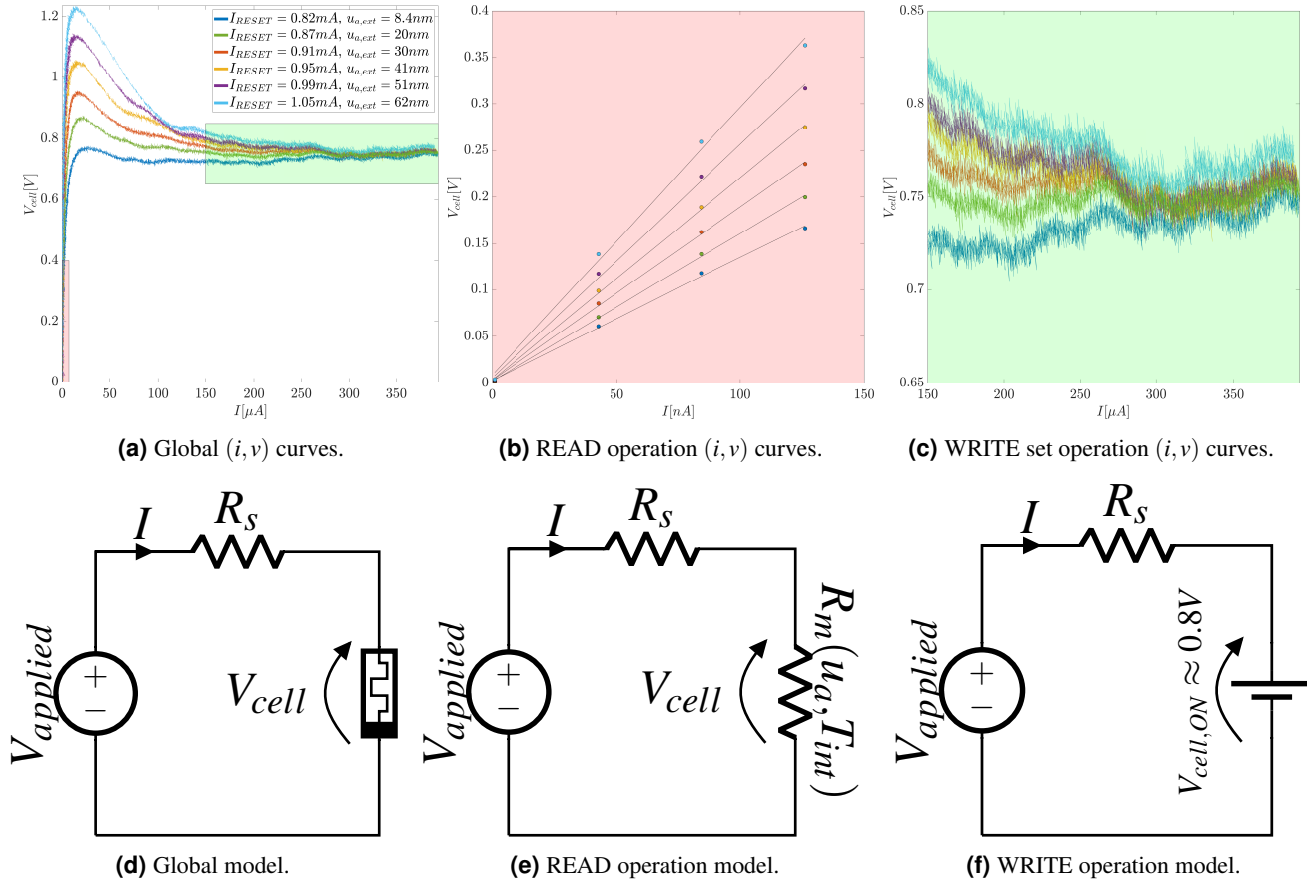


**Figure 5.** (a) DSO measured  $I - V_{cell}$  characteristics of a GST PCM cell, reset with different reset currents  $I_{RESET}$ , showing the same plateau  $V_{cell}$  value for  $I \geq I_{th} \approx 100 \mu A$ . Driving voltage  $V_{applied}$  supplied by an Arbitrary Waveform Generator through a series resistor  $R_S \approx 5.7 k\Omega$ .  $V_{cell}$  responses computed as  $V_{cell} = V - R_S I$ . Ramp rise time  $T_{rise} = 3 \mu s$ . (b) SMU measured low-field  $I - V_{cell}$  characteristics of the same PCM cell, reset with the same currents  $I_{RESET}$  as those on the main axes, showing an almost ideal linear behavior for very low current/voltage value. (c) Zoom-in of the write region  $I - V_{cell}$  characteristics, it is noticeable how  $V_{cell}$  is narrowly concentrated around  $0.8V$ . (d) Global model of a PCM device as a nonlinear time-variant dynamical system (e) READ domain model of a PCM device as a state-dependent linear resistor (f) WRITE domain model of a PCM device as an ideal voltage generator  $V_{cell,ON}$ .

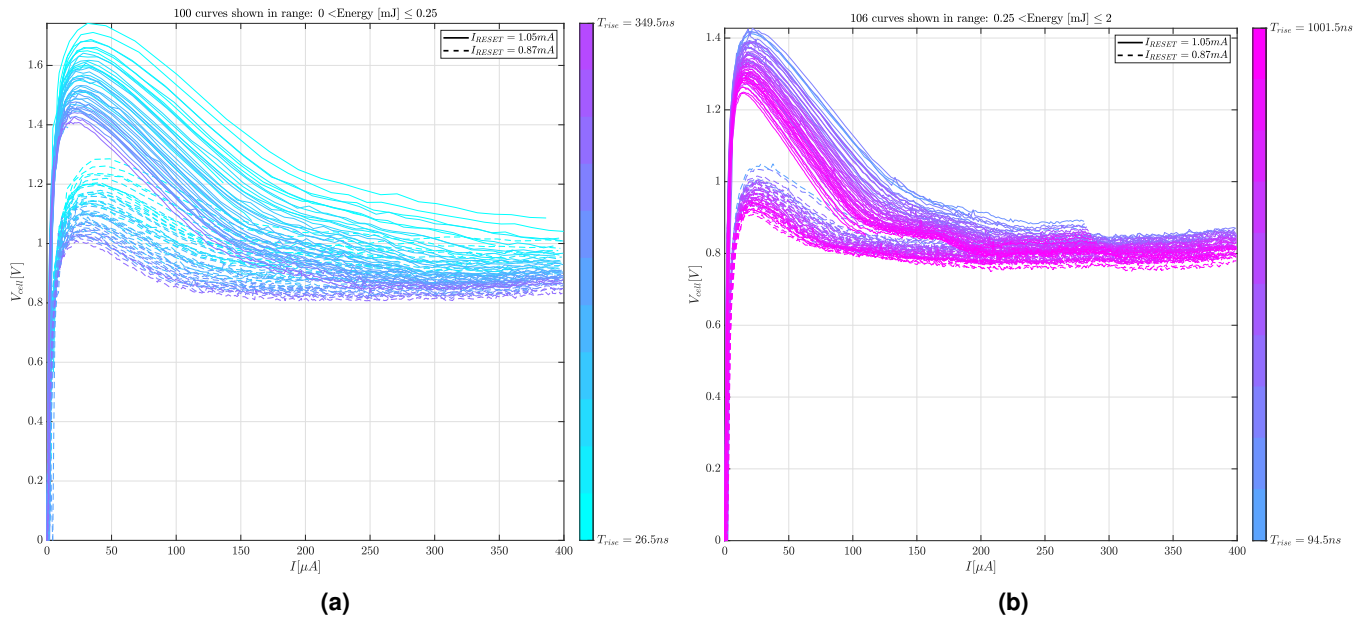


**Figure 6.** DSO measured  $I - V_{cell}$  characteristics of a GST PCM cell, reset with two different reset currents  $I_{RESET}$ , driven by a voltage ramp  $V$  supplied by an Arbitrary Waveform Generator through a series resistor  $R_S \approx 5.7k\Omega$ .  $V_{cell}$  responses computed as  $V_{cell} = V - R_S I$ . Rise times  $T_{rise}$  spanning in the range  $[26.5, 1001.5]ns$  and supplied voltages  $V$  in the range  $[1, 4]V$ . Energy estimated as the trapezoidal approximation of the integral of the dissipated power  $P = V_{cell}I$  along the curve from  $(I, V_{cell}) = (0, 0)$  up to the threshold switching peak. In **(a)** the  $I, V_{cell}$  characteristics for the PCM cell when not sufficiently heated. The final  $V_{cell}$  plateau in **(a)** varies substantially. In **(b)** the  $I - V_{cell}$  characteristics for the PCM cell when sufficiently heated. The final  $V_{cell}$  plateau in **(b)** results to be narrowly centered around  $V_{cell,ON} \approx 0.8V$ .

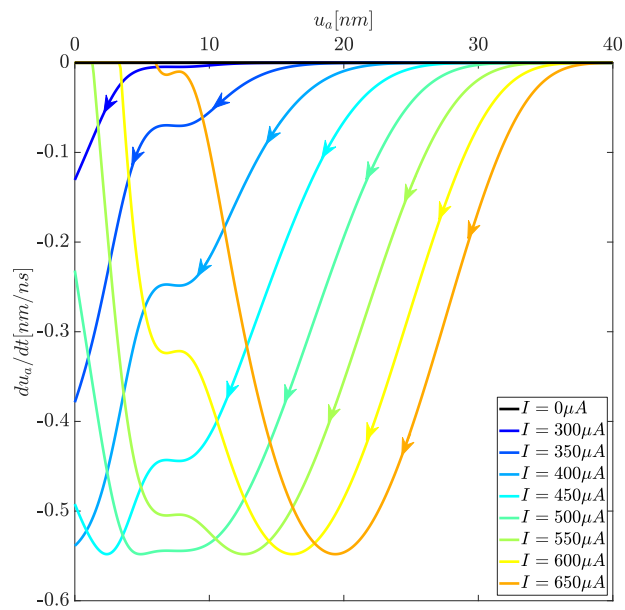


**Figure 7.** DRM computed, for a fully switched PCM Amorphous Mushroom cell in the blocked-BE condition, by means of the proposed write model parameterized on various levels of injected current  $I$ .

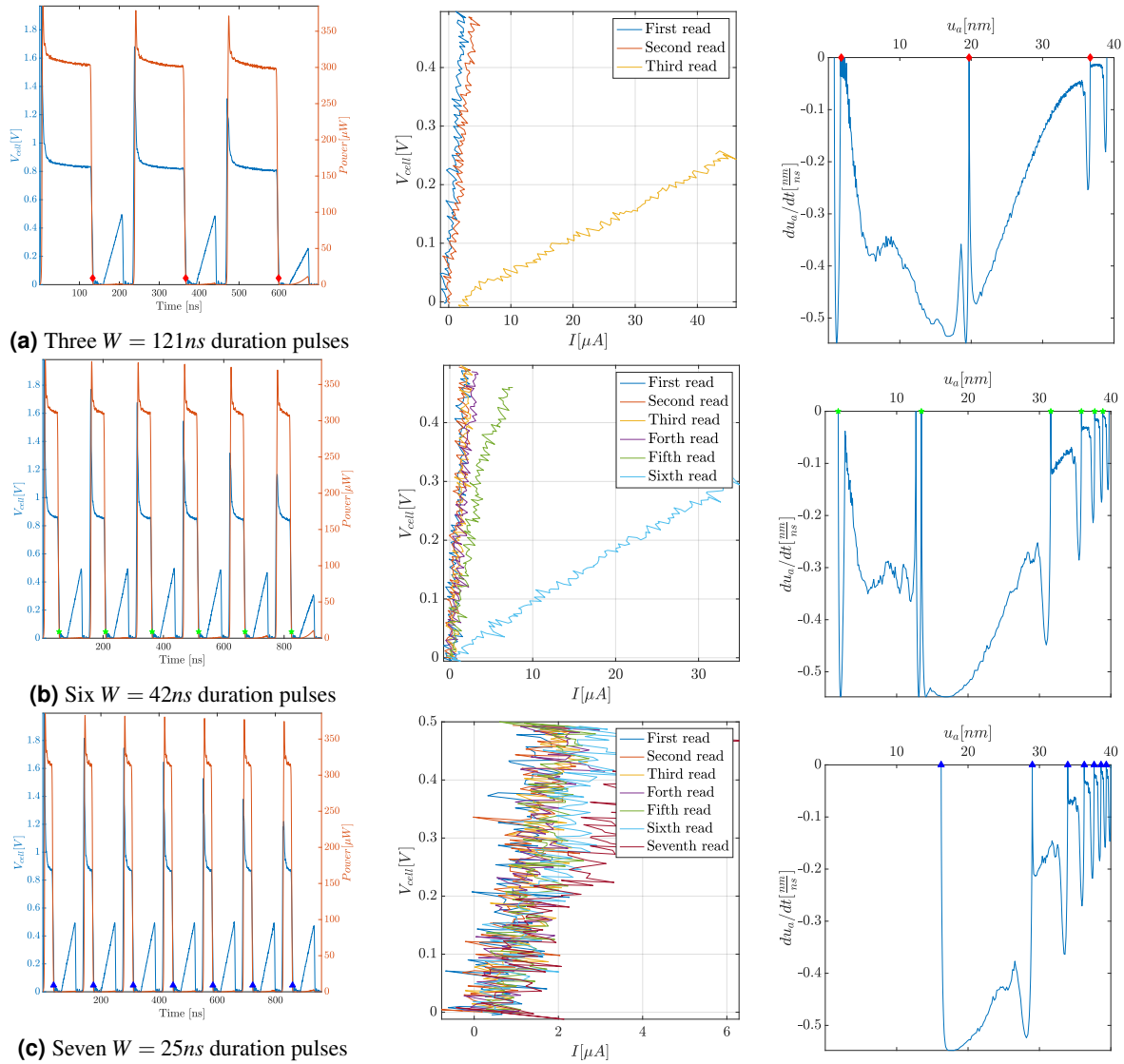


**Figure 8.** (Left Column) Collection of experimentally measured cell voltage drops  $V_{cell}$  and the corresponding absorbed electrical  $Power$  for varying write pulse duration  $W$ . Each square high-current write pulse is interleaved with a below threshold triangular read pulse. (Center Column) Collection of measured read pulses represented on the current-voltage plane for varying pulse duration  $W$ . The stored memory state  $u_a$  is here directly proportional to the slope of each curve being this a measure of the resistance state. (Right Column) Dynamic Routes, for varying pulse duration  $W$ , computed by means of the proposed model using as input the measured power signal on the left column.

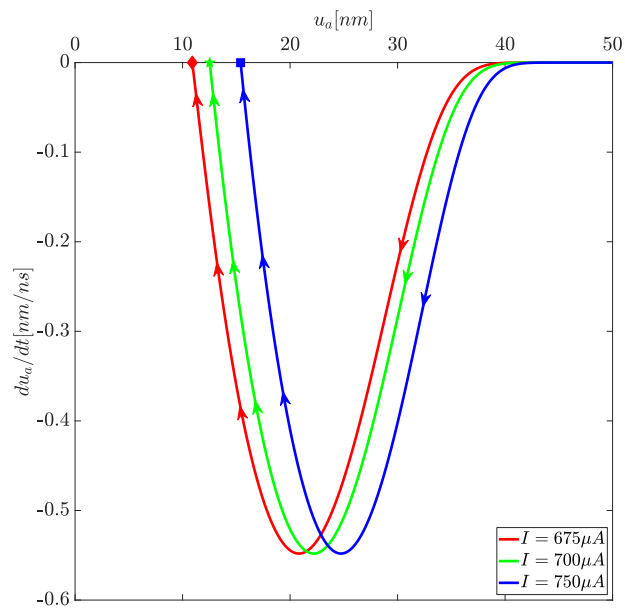


**Figure 9.** Three dynamic route maps parameterized on different SET current values. Each route, when travelled, leads to a distinct nonzero equilibrium of the first order dynamic state variable  $u_a$ .

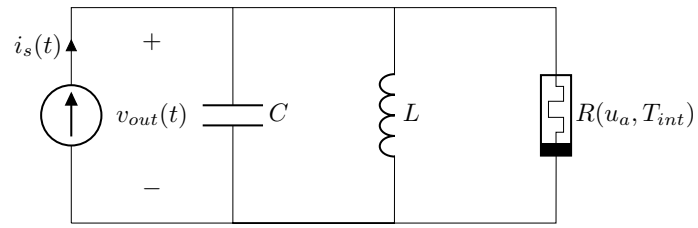


**Figure 10.** Passive tunable RLC passband filter exploiting a PCM cell in its read region via  $R_m(u_a, T_{int})$ .

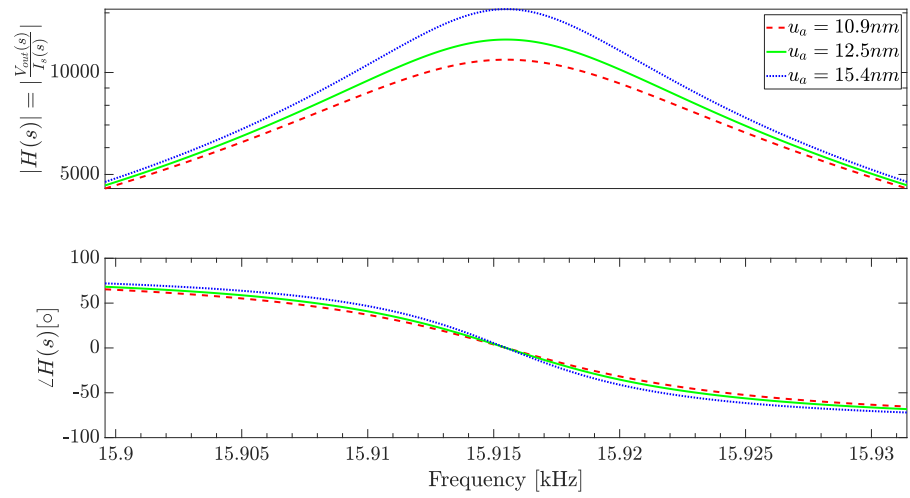
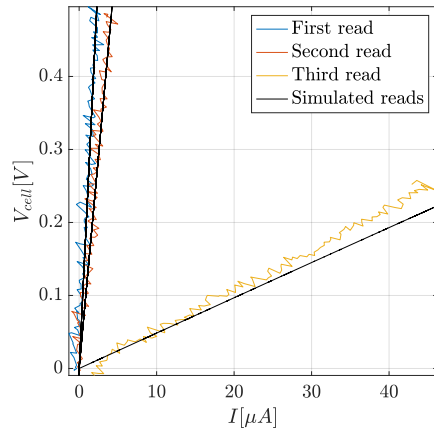
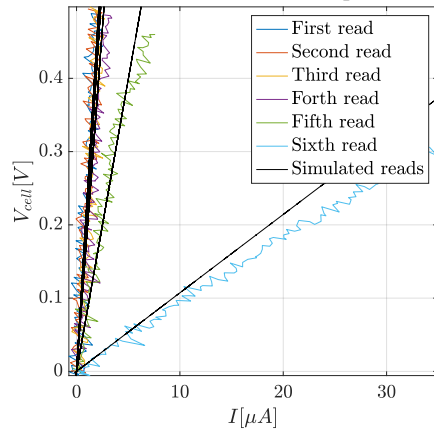


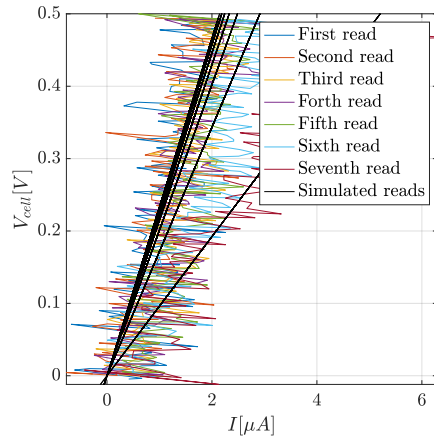
**Figure 11.** Bode plots of the transfer function  $H(s)$  parametrized on the final values reached by following the DRMs in Figure 9



(a) Three  $W = 121ns$  duration pulses



(b) Six  $W = 42ns$  duration pulses



(c) Seven  $W = 25ns$  duration pulses

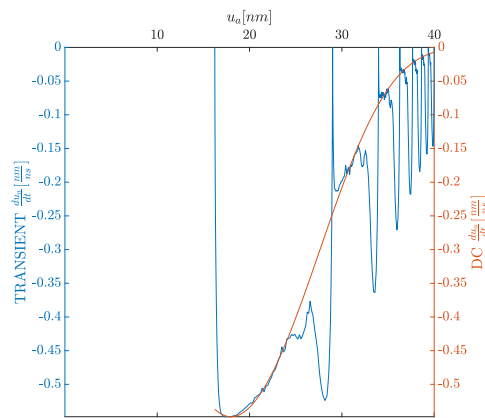
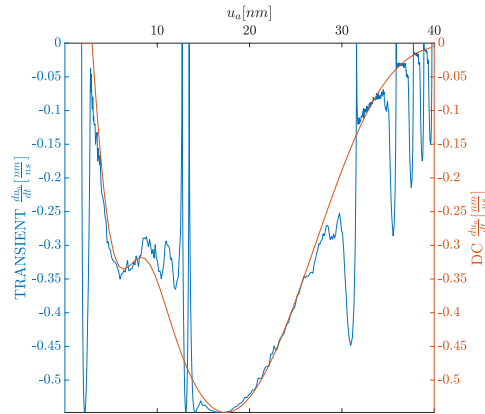
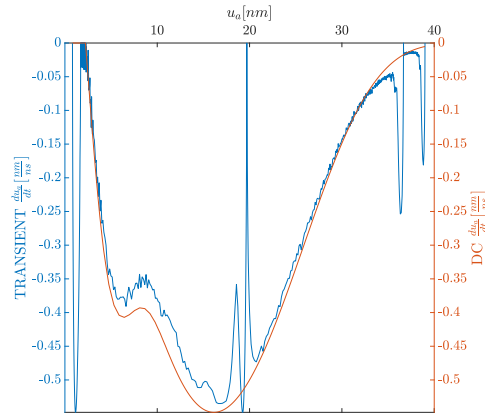


**Figure 12.** (Left column) Matching between the measured read pulsed on the voltage–current plane, as reported in the central column of Figure 8, and the expected voltage–current curves as obtained by the same dynamical simulation generating the dynamic routes in the right column of Figure 8. (Right column) Superposition of the computed dynamic routes, as reported in Figure 8, and the dynamic routes computed for a constant input power. The former are shown on the left axis as the TRANSIENT dynamic routes while the latter are on the right axis as the DC dynamic routes. The value of the constant input power used to compute the DC dynamic routes is the average measured delivered power during the write pulses plateau as reported in Figure 8.